ROYAL SOCIETY
OF CHEMISTRY

PAPER

Check for updates

Functionalization of transparent conductive oxide electrode for TiO$_2$-free perovskite solar cells†

P. Topolovsek,[ac] F. Lamberti,*[a] T. Gatti,[b] A. Cito,[a] J. M. Ball,[a] E. Menna,[b] C. Gadermaier [iD][cd] and A. Petrozza [iD] *[a]

Many of the best performing solar cells based on perovskite-halide light absorbers use TiO$_2$ as an electron selective contact layer. However, TiO$_2$ usually requires high temperature sintering, is related to electrical instabilities in perovskite solar cells, and causes cell performance degradation under full solar spectrum illumination. Here we demonstrate an alternative approach based on the modification of transparent conductive oxide electrodes with self-assembled siloxane-functionalized fullerene molecules, eliminating TiO$_2$ or any other additional electron transporting layer. We demonstrate that these molecules spontaneously form a homogenous monolayer acting as an electron selective layer on top of the fluorine doped tin oxide (FTO) electrode, minimizing material consumption. We find that the fullerene-modified FTO is a robust, chemically inert charge selective contact for perovskite based solar cells, which can reach 15% of stabilised power conversion efficiency in a flat junction device architecture using a scalable, low temperature, and reliable process. In contrast to TiO$_2$, devices employing a molecularly thin functionalized fullerene layer show unaffected performance after 67 h of UV light exposure.

1. Introduction

Perovskite solar cells (PSCs) made by using low-cost fabrication techniques have already exceeded the threshold of 20% stabilised efficiency.[1–4] Thus, they have the potential to enable a reduction in the cost of generating electricity from sunlight in comparison to conventional material systems. However, significant effort is still required in the development of device architectures that can guarantee reliable and cost effective solar cells in order to move these promising lab-scale results towards quick industrial scale-up.

Anatase titanium dioxide, processed as a compact (cTiO$_2$) and/or mesoporous layer, is a wide band-gap semiconductor often used as the electron transporting layer (ETL) in standard structured PSCs because its electronic structure supports efficient collection of photoexcited electrons from the perovskite conduction band, whilst the large valence band offset blocks holes effectively.[3,5] However, it usually requires high temperature sintering (at least 450 °C),[6] induces electrical instabilities reflecting in the current–voltage hysteresis,[7–9] and causes degradation of solar cells' power output under the illumination of the ultraviolet (UV) solar spectrum region.[10,11] The limitations of TiO$_2$ based ETLs can be partly avoided by additional interfacial thin films of fullerenes,[12] their derivatives[13–21] or other organic layers.[22] Another approach is to completely replace the metal oxide ETLs with fullerene based organic layers either as a standalone,[14,23–28] multilayered films[29–31] or in the form of a bulk heterojunction with the light harvesting layer.[32–35] From the point of view of the deposition method, organic layers are mostly spin coated, however, thermal deposition in vacuum[14,16,23,28,31] and dip coating with self-assembly were also demonstrated as promising alternatives.[22,36–38]

Apart from the incorporation in a standard device structure, phenyl-C61-butyric acid methyl ester (PC$_{61}$BM) and other fullerene based molecules found their use in highly efficient inverted perovskite solar cells.[39–51] The main reasons behind the use of fullerene based molecules are their good electron transporting properties in conjunction with the ability of interface trap states passivation, improving the charge extraction and consequently reducing electrical instabilities in the form of J–V hysteresis.[32,33,52,53]

One of the key challenges for the fully solution-based preparation of solar cells employing organic layers, such as fullerenes, is ensuring that the subsequent processing steps do not damage layers processed earlier in the fabrication procedure. Since in the standard n–i–p architecture the perovskite is most

[a]Center for Nanoscience and Technology, Istituto Italiano di Tecnologia, Via Pascoli 70/3, 20133 Milano, Italy. E-mail: francesco.lamberti@dei.unipd.it; annamaria.petrozza@iit.it

[b]Department of Chemical Sciences, University of Padova, Via Marzolo 1, 35131 Padova, Italy

[c]Jozef Stefan International Postgraduate School, Jamova cesta 39, 1000 Ljubljana, Slovenia

[d]Jozef Stefan Institute, Jamova cesta 39, 1000 Ljubljana, Slovenia

† Electronic supplementary information (ESI) available. See DOI: 10.1039/c7ta02405c

commonly solution processed on top of the ETL, the layer incorporating fullerenes needs to be indestructible during further processing with polar aprotic solvents, *e.g. N,N*-dimethylformamide (DMF), dimethylsulfoxide (DMSO), γ-butyrolactone (GBL) or similar, and insensitive to moderate thermal annealing. If this criterion is not met, the quality and reproducibility of the final device may be greatly reduced due to the dissolution of the fullerene film.[24] Last, but not least, solution deposition methods for C60 and its derivatives must minimize the consumption of expensive materials by using low-waste deposition methods and applying ultrathin layer thicknesses, making dip coating, supported by the self-assembly of organic layers on top of the substrate, the most suitable deposition technique. Control of the material consumption and the film thickness is of paramount importance for the reduction of parasitic absorption within a device and the overall costs of the large-scale device manufacturing.

The aforementioned processing challenges have been so far approached by covalent binding of fullerene derivatives or other molecules to the TiO₂ (ref. 22 and 37) or SnO₂ surface.[38] Another possible solution would be a direct functionalization of the underlying transparent electrode. One of the most used methodologies for the covalent modification of conductive ceramics such as tin-doped indium oxide (ITO) and fluorine-doped tin oxide (FTO) is the silanization technique. Silane molecules are generally cheap, easy to handle, and can be quickly bound to oxygen containing substrate surfaces using standardized recipes either *via* dip coating, spray coating or chemical vapor deposition, which makes the silanization approach a well-recognized technology in industrial coating applications.[54] The silanized layers show long-term stability to moisture, UV, heat and solvent resistance once cured, together with a good adhesion to many different substrates.[55,56] By controlling the humidity conditions during the process, it is possible to tune the thickness of the functional layer, from a monolayer (dry conditions) to a thick cross-linked multilayer (humid conditions).[57] Of course, this can alter the chemical and electronic properties of the modified substrate as well as the processability and quality of the coating.

Some of us have already demonstrated the possibility of decorating C60 with alkyl siloxane moieties by employing azomethine ylides cycloaddition reactions and subsequently of covalently modifying silica nanoparticles and films with good yields.[56,58] Recently, Wojciechowski and co-workers presented the use of a crosslinked silanized fullerene molecule, creating a thick (10 nm) fullerene layer as an ETL for PSCs.[59] The crosslinking of the spin coated silanized fullerene layer was in their case initiated by exposing the layer to vapors of trifluoroacetic acid.

Here we show, for the first time, the possibility of a direct functionalization of the semitransparent electrode by the formation of an electron transporting layer through a silanization-promoted self-assembled monolayer of functionalized fullerene molecules, overcoming the use of thick charge selective layers provided by other deposition techniques. By using a scalable dip coating technique, we demonstrate the fabrication of a conformal, chemically robust layer resulting in efficient and stable solar cells with reproducibility comparable to analogously prepared cells based on a spin-coated C60 layer, without the use of TiO₂ or any other additional material as ETL.

2. Experimental section

Device fabrication

Glass substrates coated with fluorine-doped tin oxide (FTO, 10 Ohm per sq) were successively cleaned in a Hellmanex solution (1 vol% in de-ionized water), de-ionised water, acetone and 2-propanol by ultrasonic agitation. Afterwards they were treated with O₂ plasma for 10 min. Sil-C60 SAM treatment: silanization of the substrates was carried out in a dry box at a relative humidity below 10%. Clean substrates were dipped inside a 0.1 mg ml⁻¹ Sil-C60 solution in anhydrous toluene (Sigma-Aldrich-244511) for 45 min at 50 °C. Later the substrates were rinsed with anhydrous toluene twice and dried on the hotplate at 110 °C for 20 min. For comparison, Sil-C60 SAM samples in humid air under the fume hood were prepared following the same procedure just described. The relative humidity inside the fume hood during the FTO modification was above 60%.

Thin films of pristine C60 were prepared by spin coating 10 mg ml⁻¹ C60 (Solenne 99.5%) solution in 1,2-dichlorobenzene (Sigma-Aldrich-240664) at 4000 rpm for 30 s on clean FTO substrates immediately after the 10 min O₂ plasma treatment. The substrates were subsequently annealed at 110 °C for 20 min. These steps were performed in a nitrogen-filled glove box.

The compact TiO₂ layer was prepared by spin coating compact TiO₂ precursor on top of a clean and O₂ plasma treated FTO at 2.000 rpm, subsequently sintered on a hotplate at the temperature of 500 °C for 45 min. The precursor was prepared by mixing titanium(IV) isopropoxide (Sigma-Aldrich 377996) with anhydrous 2-propanol (Sigma-Aldrich 278475) in a 1 : 8 volume ratio, adding 4.5 μl of 2 M HCl per 1 ml of precursor mixture.

The perovskite precursor solution for the SEM morphological study was prepared by mixing 1 M solutions of cesium lead triiodide (CsPbI₃) and formamidinium lead triiodide (FAPbI₃) in a 0.175 : 0.825 volume ratio. CsPbI₃ and FAPbI₃ were prepared by mixing equimolar amounts of CsI (Sigma-Aldrich 203033) and PbI₂ (Alfa Aesar 12724) and FAI (DYESOL 879643-71-7) and PbI₂ respectively. Both precursor solutions were prepared in a solvent mixture of anhydrous dimethylsulfoxide (Sigma-Aldrich 276855) and *N,N*-dimethylformamide (Sigma-Aldrich 227056) in a 3 : 7 volume ratio. Spin coating of the perovskite layers was done with a solvent quenching technique[60,61] in a 2-step manner, first 2000 rpm (2000 rpm per s ramp) for 10 s followed by a 5000 rpm (5000 rpm per s ramp) for 30 s. 300 μl of toluene was dripped onto the substrate after 10 s of the second step. Substrates were immediately put on a hotplate at 170 °C for 10 min.

Perovskite precursor solution for solar cells was prepared by mixing 1 M formamidinium lead bromide (FAPbBr₃), formamidinium lead iodide (FAPbI₃), cesium lead iodide (CsPbI₃), and methylammonium lead iodide (MAPbI₃) in a 0.1 : 0.65 : 0.05 : 0.2 volume ratio. FAPbBr₃ and MAPbI₃ were prepared by mixing

This journal is © The Royal Society of Chemistry 2017

J. Mater. Chem. A, 2017, **5**, 11882–11893 | **11883**

equimolar amounts of formamidinium bromide (DYESOL 146958-06-7) and lead bromide (Alfa Aesar 10720) and methylammonium iodide (DYESOL 14965-49-2) and lead iodide respectively. All precursor parts were prepared in a solvent mixture of DMSO and DMF in a 3 : 7 volume ratio, except the $CsPbI_3$, which was prepared in 3 : 2 DMSO : DMF volume ratio. Spin coating of perovskite layers for solar cells was done with a solvent quenching technique in a 2-step manner, first 2000 rpm (2000 rpm per s ramp) for 10 s followed by 5000 rpm (5000 rpm per s ramp) for 50 s. 300 μl of toluene was dripped onto the substrate after 30 s of the second step. Perovskite films were annealed at the temperature of 110 °C for 1 h. After the annealing, the substrates were left to cool down. Afterwards 2,2′,7,7′-tetrakis[N,N-di-(4-methoxyphenyl)amino]-9,9′-spirobifluorene (Spiro-OMeTAD) was spin coated at 4000 rpm (4000 rpm per s ramp) for 30 s. The solution was prepared by adding 73 mg of Spiro-OMeTAD into 1 ml of chlorobenzene (Sigma-Aldrich-284513), then adding 28.8 μl of 4-tert-butylpyridine (Sigma-Aldrich-142379) and 17.5 μl of 520 mg ml^{-1} bis(trifluoromethane)sulfonamide lithium salt (Sigma-Aldrich-544094) solution in anhydrous acetonitrile (Sigma-Aldrich-271004). After the Spiro-OMeTAD deposition the samples were removed from the glovebox and left in a desiccator for 12 h to complete the Spiro-OMeTAD doping. Devices were completed with a 50 nm Au top contact, thermally evaporated at a pressure of 1×10^{-6} mbar.

Device characterization

All devices were measured under simulated AM1.5 solar illumination using a class AAA solar simulator (Oriel Sol3A, Newport). The illumination intensity was calibrated using an unfiltered certified Si reference diode (area = 4 cm^2, Newport) to be 100 mW cm^{-2} (typical spectral mismatch factor of 1.01 for solar cells based on $CH_3NH_3PbI_3$),[62] except for devices used for treatment comparison in humid and dry environment, which were measured at an intensity of 88 mW cm^{-2}. The current density–voltage (J–V) characteristics and the stability of the current/power output with time were recorded with a Keithley 2400. No light soaking or pre-biasing was applied before the J–V measurements. The calculated power conversion efficiency (PCE) curves were, only in this case, normalized to 1 sun intensity. The illuminated electrode area, defined with a black anodized aluminium mask, was 9.38 mm^2. Devices were measured under lab atmosphere conditions at 23 ± 2 °C and 30% relative humidity.

The stability of the solar cells to ultraviolet (UV) light exposure was tested by storing the devices in a nitrogen filled glovebox (equivalent to a perfect encapsulation against oxygen and water). Devices were exposed to a 36 W UV lamp, or kept in the dark as a control. The spectral irradiance of the UV lamp (presented in Fig. S13†) was measured using an Ocean Optics MAYA 2000 Pro (spectrally calibrated using a quartz-tungsten-halogen irradiance standard, Newport) and corrected to absolute units by measuring the short-circuit of a certified unfiltered Si reference diode (Newport) of known spectral responsivity. To measure their performance, the devices were periodically removed from the glovebox temporarily for measurements using the aforementioned solar simulator, and then immediately returned.

Electrochemical characterization

Cyclic voltammetry (CV) was performed using a potentiostat/galvanostat PGSTAT302N (Ecochemie, MetroOhm) in acetonitrile (ACN) solutions with 5 mM ferrocene as redox probe and 0.1 M tetrabutylammonium tetrafluoroborate (TBATFB) as electrolyte. A platinum counter electrode (Amel) and a Ag/AgCl (KCl sat) reference electrode (Mettler Toledo) were used. The working electrode was a bare FTO or a Sil-C60 SAM sample masked with a kapton tape shaping 0.025 cm^2 active area. Measurements were performed at room temperature in standard conditions. The scan rate was 0.025 V s^{-1}. At least three CV scans were collected and the last one is shown in the manuscript. Electrochemical impedance spectroscopy (EIS) measurements were performed using the Frequency Response Analyzer (FRA) module of the potentiostat, biasing samples at 0.46 V (versus Ag/AgCl) with 5 mM ferrocene in ACN, using a perturbation signal of 10 mV scanning frequencies from 1 MHz to 0.1 Hz. NOVA 1.11 software was used for fitting FRA experimental data and analyzing CVs.

Computational details

Density functional theory (DFT) calculations, including full geometry optimization and generation of the surface plots of the HOMO and LUMO orbitals, were carried out using the Gaussian 09 program (revision B.01).[63] The hybrid B3LYP functional and the 6-311G(d,p) basis set were employed.
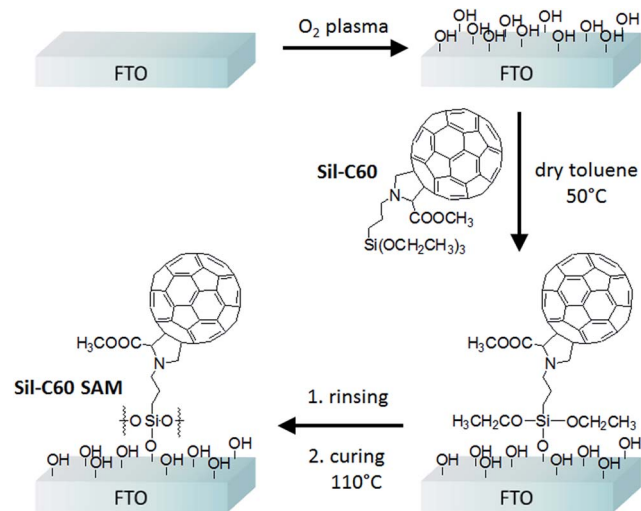
Wettability measurements

An OCA 15 EC system was used for the study of the contact angle of water drops on different substrates. Measurements were carried out by the sessile drop method. The volume of the water droplet used for determination of contact angles was 1 μl. Digital images were captured with a CCD-camera with a resolution of 752 × 582 pixels. The image is elaborated by the software SCA-20, in order to define the exact value of the contact angle.

SEM image grain size analysis

Grain size analysis was performed using Gwyddion 2.40 software, using watershed grain analysis and related statistical tools.[64] Error bars are given by averaging 4 different samples for each condition.

3. Results and discussion

In Scheme 1 we report the anchoring mechanism of N-[3-(triethoxysilyl)propyl]-2-carbomethoxy-3,4-fulleropyrrolidine, hereby named as Sil-C60, on bare FTO. The synthesis of Sil-C60 has been carried out following a slightly modified procedure with respect to the one previously reported by some of us, allowing a higher yield, as reported in the (ESI†).[56] Self-assembly of Sil-C60 on the surface of an FTO electrode was carried out in a low humidity environment (<10% R. H.) inside a dry box by a direct immersion of the FTO substrates in a diluted (0.1 mg ml^{-1}) Sil-C60 solution (see Experimental section). The bare FTO surface was activated by oxygen plasma (O_2 plasma) in order to

11884 | J. Mater. Chem. A, 2017, **5**, 11882–11893

This journal is © The Royal Society of Chemistry 2017

Scheme 1 Illustration of the fullerene self-assembled monolayer (Sil-C60 SAM) fabrication process, involving the covalent anchoring of Sil-C60 on an oxygen plasma-activated FTO substrate.

increase the amount of hydroxyl surface terminated groups, boosting the subsequent covalent attachment of Sil-C60. Dry conditions and quick reactions promote the self-assembly mechanism avoiding the development of thick cross-linked coatings. After a final curing step at a relatively low temperature (110 °C), an FTO surface covalently modified with a self-assembled monolayer of functionalized C60 molecules was obtained, defined from now on as Sil-C60 SAM.

We assessed the chemical stability of the functionalization by comparing the FTO/Sil-C60 SAM substrate with a solution-

Fig. 1 Wettability measurements on FTO modified surfaces with Sil-C60 (Sil-C60 SAM) and solution processed fullerene (C60 spin coated). (a and c) refer to as-deposited samples while (b and d) denote samples after 5 min immersion in a hot DMF bath; (e) refers to a bare FTO used as a reference sample. The volume used to form water droplets was 1 μl.

processed C60 layer. In particular, we measured the water contact angles of the modified substrates before and after the treatment of the substrates in a hot (120 °C) DMF bath, thus simulating potentially damaging conditions for such an organic layer during the perovskite processing. Similar conditions have been used, for example, in the hot casting technique[65,66] or a 2-step perovskite deposition technique where precursor solutions were used at an elevated temperature.[67] The results are summarized in Fig. 1 and Table 1, where we show the wettability images and a summary of fitted contact angles, respectively.

As highlighted in Table 1, the Sil-C60 SAM sample exhibits a high water contact angle before and after the treatment in a hot DMF bath, while the spin coated C60 fullerene sample shows a notably reduced contact angle after the treatment, with a value which is smaller than that of a bare FTO. This is probably due to highly polar DMF molecules remained chemisorbed on the surface, increasing the hydrophilicity of the substrate. These results confirm the robust covalent origin of the bond between Sil-C60 and FTO, whereas in the case of spin coated C60 the layer is only weakly interacting with the surface, which results in its nearly complete dissolution after hot solvent treatment. Moreover, the relatively high standard deviation of the contact angle value before DMF treatment for the C60 spin coated sample reveals an intrinsic inhomogeneity of the surface coverage following fullerene processing, which may affect the reproducibility of solar cells built upon.

Before proceeding in the PSCs development, and in order to gather information on the thickness and surface coverage of the FTO by the Sil-C60 SAM before and after the DMF treatment, we tested the functionalized substrate through cyclic voltammetry (CV) and electrochemical impedance spectroscopy (EIS). Experimental details on electrochemical measurements are given in the Experimental section. First, the barrier effect towards the diffusion of a charged redox probe in solution after electrode modification was studied by CV (Fig. 2a).[68] Here, the positively charged redox probe (ferrocene) is employed to assess the faradic response of a bare FTO electrode and of a functionalized one. The CV clearly shows a quasi-irreversible electrochemical process occurring at the bare FTO surface ($\Delta E = 0.24$ V), whereas almost no faradic current is detected when performing CV on Sil-C60 SAM under the same conditions. These results suggest a complete modification of the FTO surface by the Sil-C60 molecules.[69] Stability tests, *i.e.* several CVs in acetonitrile (ACN), confirm the chemical and electrical resistance of the modification (Fig. S1†).

Electrochemical impedance spectroscopy (EIS) also allows characterization of the thickness of the fullerene layer. A simple
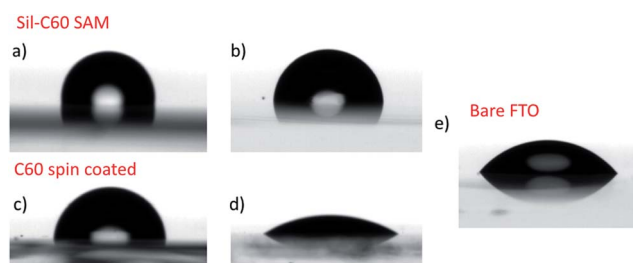
Table 1 Summary of wettability measurements on samples shown in Fig. 1. Error bars refer to at least five repetitive measurements on the same sample in different areas and three different substrates per type

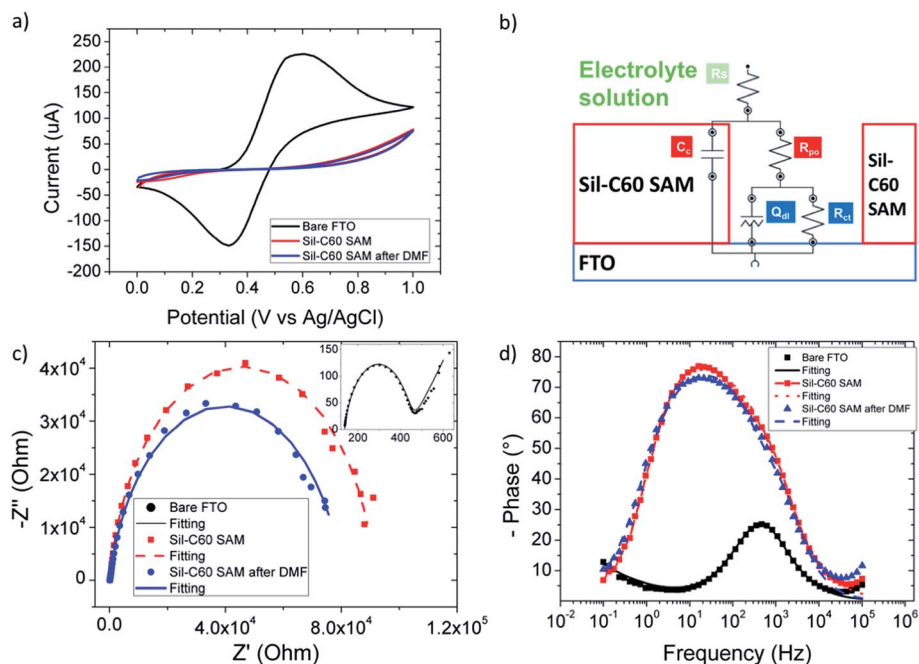|	Contact angle as deposited (°)	Contact angle after DMF treatment (°)	Relative decrease (%)
Sil-C60 SAM	98 ± 3	85 ± 0.5	11%
C60 spin coated	76 ± 10	19.7 ± 0.5	74%
Bare FTO	53 ± 1	—	—

Fig. 2 Electrochemical characterization of Sil-C60 SAM before and after DMF treatment and bare FTO. (a) Cyclic voltammetry (CV) with a ferrocene redox probe (5 mM in ACN solution); (b) equivalent circuit for defective Sil-C60 SAM used for the fitting of experimental impedance data in panel (c and d); (c) Nyquist plot and (d) Bode phase plot of Sil-C60 SAM sample; the inset graph in (c) shows Nyquist plot of the bare FTO sample. CVs were performed at 25 mV s⁻¹ (reference electrode: Ag/AgCl; electrolyte: TBATFB 0.1 M in ACN; EIS performed at 0.46 V *versus* Ag/AgCl with 5 mM ferrocene). Fitted parameter values are shown in Tables S1 and S2.†

equivalent circuit model is used for fitting the experimental data and is presented in Fig. 2b. This circuit is often used for modeling damaged thin coatings in corrosion studies.[70,71] R_s represents the solution resistance, R_{po} is the ion resistance through the coating (pores or pinholes present within the coating), C_c is the capacitance related to the ion accumulation at the surface of the intact coating, R_{ct} is the charge transfer resistance between the electrolyte and the FTO, and Q_{dl} is a constant phase element (CPE) related to the pseudo-double layer capacitance at the FTO surface.[72] Tables S1 and S2† summarize all of the fitted values for the different samples. It is possible to determine the thickness of the coating starting from Q_{dl} and to estimate the surface coverage starting from R_{ct}.[73] Therefore, by fitting the experimental data in Fig. 2c and d, coating capacitance values of C_c = 649 nF and 675 nF are obtained for the Sil-C60 SAM sample and Sil-C60 SAM sample treated with DMF respectively. Using eqn (S1†) it is possible to obtain information about the thickness of the coating, by knowing the dielectric constant of the coating. Assuming a value that should be similar to a bare fullerene and PCBM (3.9–4.5)[74] we obtained a nominal thickness for the silane layers of approximately 1.4 ± 0.2 nm substantially unchanged before and after DMF treatment. Moreover, the surface coverage calculated with eqn (S2†),[72] is estimated to be 99.5%, a result in agreement with CV outcomes. The Nyquist plot in Fig. 2c and the Bode phase plot in Fig. 2d offer a complete view of the mechanisms involved in the electrochemical reaction at the electrode interface. The bare FTO (black curve in the inset graph in Fig. 2c) exhibits behavior consistent with a modified Randles

cell: one semicircle at higher frequencies, *i.e.* a single time constant for the phenomenon; and a well-defined Warburg diffusion element in the circuit at low frequencies.[75] In contrast, the Sil-C60 SAM modified FTO samples show elliptical semicircles with larger radii, thus we can assume the existence of two distinct time constants originating from different phenomena. In agreement with the time constants obtained by fitting the electrical circuit model in Fig. 2b, two RC contributions are found (Fig. 2d, blue curve): the main peak at lower frequencies (at about 10 Hz) is assigned to the charge transfer reaction at the interface between the solution and the coating (*i.e.* the actual electrochemical reaction taking place at the modified real interface), whereas the higher frequency peak (at about 1 kHz) is due to an electrochemical reaction taking place at the surface of the underlying FTO electrode, quite similar to the bare FTO resonance peak (black curve in Fig. 2d). We can then conclude that the slower phenomena (*i.e.* the ones at lower frequencies) occurring at the modified interface are the limiting electrochemical reactions occurring at the modified electrode, thus explaining the lack of faradic current in CV in Fig. 2a.

To develop a model for a better description of the Sil-C60 SAM morphological properties we performed Density Functional Theory (DFT) calculations (B3LYP/6-311G**, see Experimental section for details) on isolated Sil-C60. The calculations revealed a distance of 1.46 nm between the plane containing the three oxygen atoms bound to Si and the furthest parallel plane containing C atoms on the C60 moiety (see Fig. 3). Based on this estimation and on the outcome of our electrochemical study, which provided a value of 1.4 nm for the thickness of the
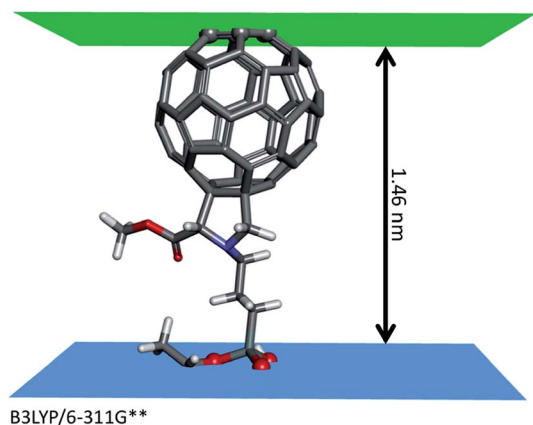
Fig. 3 Minimized geometry of Sil-C60, as calculated through DFT, highlighting the distance between the siloxane oxygen atoms and the opposite edge of C60 (see text).

fullerene-based layer on top of FTO, we can infer the presence of a Sil-C60 monolayer covering the FTO surface, that remains unchanged after the DMF treatment.

Together, EIS and wettability measurements performed on the Sil-C60 SAM sample (Table 1) suggest a high yield of modification throughout the FTO surface with Sil-C60 molecules with small contact angle deviations over the various spots examined, showing the formation of a conformal and strongly hydrophobic surface. Significant change in the wettability of the anode surface due to the presence of a homogeneously distributed fullerene layer is likely to considerably influence the process of perovskite growth during device realization.

In order to understand whether the altered surface properties of various substrates influence the perovskite growth mechanism, we deposited thin perovskite films by spin coating a mixed cation $Cs_{0.175}FA_{0.825}PbI_3$ precursor,[76] using a solvent quenching technique (see Experimental section for experimental details). We acquired both cross section and surface morphology SEM images of perovskite films deposited on O_2 plasma treated bare FTO (Fig. 4a and d), FTO covered with

compact TiO_2 (Fig. 4b and e) and FTO covered with Sil-C60 SAM (Fig. 4c and f). Software analysis of surface morphology SEM images shows a gradual increase of the average grain size from bare FTO (250 nm), to FTO covered with compact TiO_2 (270 nm) and then to FTO modified by Sil-C60 SAM (300 nm). Cross section images revealed smaller crystallites interconnected into a quasi-continuous film on the bare FTO and compact TiO_2 covered FTO. In the case of a perovskite layer formed on Sil-C60 SAM modified FTO, single perovskite grains proceed from the top to the bottom of perovskite layer. This increase in the crystallinity may reduce the trap density of states and associated trap-assisted recombination.[77,78]

In Fig. 5 we present a correlation between the contact angle measurements and the average perovskite grain size of the analyzed films. It seems that the average grain size increases on surfaces with decreasing wettability, in agreement with observations reported previously.[79] However, in the referred work a 2-step perovskite processing method was used, while in our case a 1-step processing method with solvent quenching was employed.

Perovskite solar cells with Sil-C60 SAM, spin-coated C60, compact TiO_2 and bare FTO were fabricated in a n–i–p
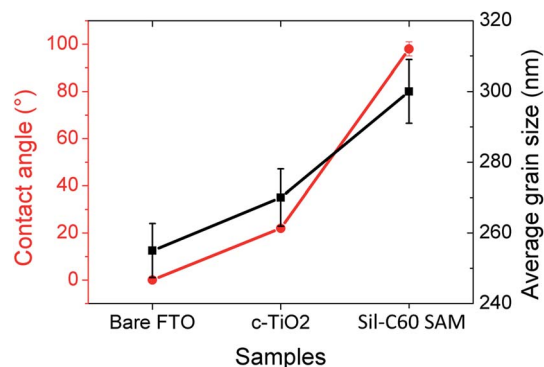

Fig. 5 Correlation between the contact angle values and the average perovskite grain size obtained on various substrates.
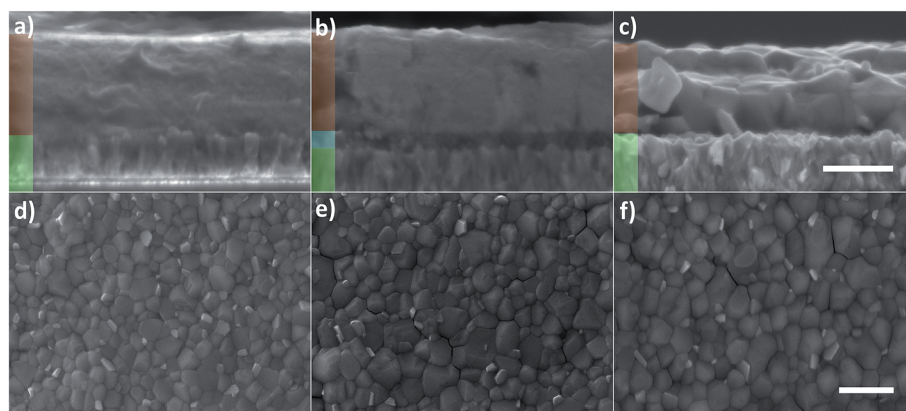

Fig. 4 Morphological characterization of perovskite films on various substrates. Cross section (a–c) and surface morphology (d–f) SEM images of perovskite films formed on a bare FTO (a and d), FTO covered with compact TiO_2 (b and e) and FTO modified by a Sil-C60 SAM (c and f). Shaded parts of cross section images mark the FTO (green), compact TiO_2 (blue) and perovskite layer (brown). The length of the scale bar for cross section images is 500 nm, for surface morphology images 1 μm.

architecture (*i.e.* the ETL is deposited on top of the transparent electrode) and tested. The active layer was a mixed cation and anion $Cs_{0.05}FA_{0.75}MA_{0.2}PbBr_{0.3}I_{2.7}$ perovskite, while Spiro-OMeTAD was used as the hole transporting material. The device top contact was a gold cathode. The choice of using a triple cation perovskite over the conventional $MAPbI_3$ was based solely on the previously demonstrated increased environmental stability and stability under constant light illumination, providing equally high or even improved performance over $MAPbI_3$.[4,80] We carried out a coarse optimization of perovskite precursor solution, varying the halide (iodine to bromine) ratio to achieve near optimum performance of the solar cells. Fig. 6a shows the current density–voltage (*J*–*V*) characteristics of the best devices. The figures of merit of the solar cells are presented in Table 2. The results reveal that devices based on FTO covered with spin coated C60 or with Sil-C60 SAM show reduced hysteretic behavior during the voltage sweep of 50 mV s^{-1} in comparison to a conventional compact TiO_2 based device or a device without any ETL. It is well known that devices employing standalone compact TiO_2 as ETL exhibit pronounced *J*–*V* hysteresis attributed to the combined effect of the electron extraction barrier between the compact TiO_2 and

Table 2 Solar cell parameters from the best performing devices extracted from the *J*–*V* characteristics presented in a Fig. 6a

	Bare FTO		cTiO$_2$		C60 spin coated		Sil-C60 SAM	
	BWD	FWD	BWD	FWD	BWD	FWD	BWD	FWD
V_{oc} (V)	0.97	0.88	1.06	0.92	1.05	1.05	1.04	1.05
J_{sc} (mA cm^{-2})	16.8	16.7	19.0	18.9	19.5	19.4	19.4	19.2
FF	0.58	0.31	0.71	0.21	0.74	0.71	0.74	0.60
PCE (%)	10.3	5.1	14.5	3.7	15.4	14.6	15.2	12.4

the perovskite layer,[9] interface electron trapping and to dynamic interface changes caused by the build-up or back-drift of ions upon application of electric field.[81] In order to determine the steady state performance of solar cells regardless of the voltage scan rate, we tracked the power conversion efficiency (PCE) over time at a fixed applied voltage near the maximum power point (MPP) for each device, as shown in Fig. 6b. Sil-C60 SAM and spin coated C60 employing devices show stable temporal photocurrents, reaching up to 15% PCE in both cases. The sample with FTO only and with compact TiO_2 (cTiO$_2$) layer show lower
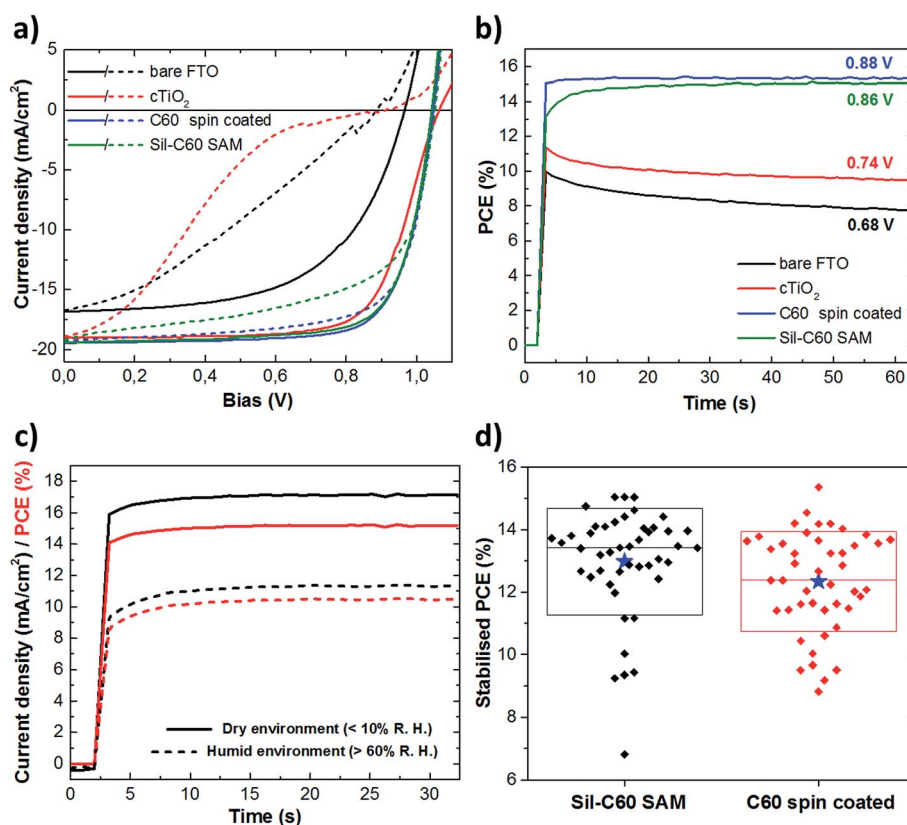

Fig. 6 Perovskite solar cell characterization. (a) *J*–*V* characteristics of devices prepared with no or with various ETLs (as indicated in the legend), presenting backward (solid line) and forward (dashed line) voltage scan direction, measured with a scan rate of 50 mV s^{-1} at the intensity of 1 sun. (b) Stabilised power conversion efficiency of the best devices measured at the maximum power point. (c) Stabilised photocurrents (black lines) and PCEs (red lines) of a typical Sil-C60 SAM based device prepared in either dry (solid curves) or humid environment (dashed curves), measured at the maximum power point of 0.76 V and 0.8 V respectively. (d) Stabilised PCEs device statistics on Sil-C60 SAM and spin coated C60 as ETLs obtained after 60 s of illumination near the maximum power point. A star symbol marks the average value and the box encloses measurements within the standard deviation. The horizontal line inside the box marks the median value. The size of the illuminated area of all devices was 9.38 mm^2.

starting performances at the MPP and a reduction over time. Although we carried out a perovskite layer optimization, we believe that there is still room for improvement in solar cell performance of fullerene based devices, especially in achieving higher photocurrents by fine-tuning perovskite layer thickness, chemical composition and the whole process of spin coating. Still, stabilised PCEs obtained with the Sil-C60 SAM employing solar cells demonstrate improved or comparable performance to other standard structured, fully solution processed PSCs where organic based ETLs are deposited by techniques with increased material consumption.[24,26,35,59] We attribute formidable performance of Sil-C60 SAM to a combined effect of efficient electron extraction properties of fullerene based molecules, beneficial influence on perovskite film formation and thickness dependent parameters, such as lower series resistance and parasitic absorption. The latter property marks Sil-C60 SAM as the most rational choice for tandem solar cells, where minimal parasitic absorption is sought for.

How effective is the anchoring of the functionalized fullerene molecule depends on the substrate surface termination groups and the environment in which the self-assembly is carried out. To evaluate the preferred treatment conditions, we performed the Sil-C60 self-assembly onto FTO in a dry (<10% R. H.) or humid (>60% R. H.) environment. As presented in Fig. 6c, devices produced in humid conditions showed decreased performance in terms of stabilised photocurrent and PCE at the maximum power point. We attribute this outcome to a poor bonding of Sil-C60 in the presence of water in the atmosphere in which the treatment is performed and in the Sil-C60 solution. A high concentration of water molecules in the chemical environment favors the cleavage of Si–O–Si bonds leading to the formation of patched areas of different thicknesses. Poor charge selectivity in uncovered areas contributes to a higher recombination rate of photogenerated charges nearby the electrode, effectively reducing the extracted photocurrent.[82]

In order to evaluate the reproducibility of the solar cell fabrication, which depends mainly on the coverage of the perovskite layer and its underlying charge selective layer, we prepared and tested two large sets of devices employing Sil-C60 SAM and spin coated C60 as ETL. Each device was measured by applying a bias at the MPP (priorly determined by the 50 mV s^{-1} scan measurement, using the backward scan as the reference), tracking the photocurrent and associated power conversion efficiency in time. After 1 minute the device's PCE was taken as a stabilised value and used in the performance statistics presented in Fig. 6d. Both sets show similar dispersion of results with the mean PCE values of $13.0 \pm 1.7\%$ and $12.3 \pm 1.6\%$ for the Sil-C60 SAM and spin coated C60 based devices respectively. These results confirm that although the thickness of the Sil-C60 SAM is considerably lower than the thickness of a spin coated C60 (about 20 nm, measured by a profilometer, in agreement with the recent study),[59] it still acts as a stable electron extraction layer. This represents a significant advantage over the pristine fullerene ETL by virtue of increased chemical stability, and requiring less material using a scalable dip-coating technique. The performance statistics of compact TiO$_2$ based devices was here omitted since they did not show stabilised PCEs (Fig. S5†).
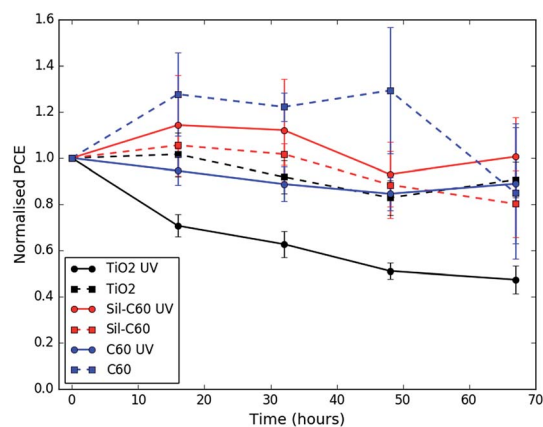

Fig. 7 Stability of the power conversion efficiency (higher efficiency scan direction, open-circuit to short-circuit) of devices fabricated with different electron transport layers over time, with or without continuous UV exposure with a 36 W lamp, as indicated in the legend.

Finally, we have performed some preliminary experiments to evaluate the stability of each of the electron transport layers to ultraviolet light exposure under inert conditions. This experiment is important because the UV portion of sunlight commonly causes continuous solar cell degradation[83] in particular in devices employing TiO$_2$, which has known issues involving the formation of deep lying surface defects.[10,11] Devices were exposed to UV light continuously for 16 h in the glove box and subsequently measured under the solar simulator in normal atmosphere. The procedure was repeated for four consecutive days, with the exception of the increased illumination time on the last day (19 h), which amounted to total 67 h of UV light exposure. At that point significant differences in performance change appeared between the samples. The current density–voltage characteristics of all the pixels used with increasing cumulative UV exposure (or storage time in an inert atmosphere for the controls) are given in the ESI Fig. S8–S12.† The final results are summarized in Fig. 7 where the average power conversion efficiency normalized to the initial values of 6–8 pixels are shown for the higher efficiency scan direction (the trends for the other device parameters and opposite scan direction are given in Fig. S6 and S7†). We observe that the power conversion efficiency of all control samples (without the UV exposure) remains relatively constant over increased storage time. However, when devices with compact TiO$_2$ are exposed to UV, they exhibit continuous and rapid degradation, mainly due to a reduction in the fill factor of the backward scan direction (see ESI Fig. S6†). In contrast to compact TiO$_2$, devices employing C60 or Sil-C60 SAM show increased stability without any performance degradation after 67 h of UV exposure.

4. Conclusions

We show that functionalized fullerene molecules can covalently bind to a clean, oxygen terminated surface of an FTO electrode, forming a robust and conformal self-assembled monolayer.

This is enough to act as an efficient and reliable electron extracting layer in perovskite solar cells, reducing the current–voltage hysteresis, without the use of any conventional ETLs. The application of strongly bound fullerene molecules as an interfacial layer not only eliminates the need of any high temperature processing and increases the stability of the device to UV irradiation but also significantly simplifies large scale deposition and reduces the material consumption through the mechanism of self-assembly, which makes this approach much more attractive for industrial scale production.

Author contributions

P. T. fabricated and tested the devices. J. M. B developed the testing set-up. F. L. performed FTO modification, electro-chemical measurements and grain size analysis on SEM images; A. C. performed wettability measurements; T. G. synthesized Sil-C60, E. M. performed DFT calculations and contributed to the supervision of the work, P. T., A. P. and F. L. conceived the idea for the project and designed the experiments. A. P. supervised the work. All authors contributed to the writing of the manuscript.

Acknowledgements

References

1 S. D. Stranks and H. J. Snaith, Metal-halide perovskites for photovoltaic and light-emitting devices, *Nat. Nanotechnol.*, 2015, **10**(5), 391–402.

2 W. S. Yang, J. H. Noh, N. J. Jeon, Y. C. Kim, S. Ryu, J. Seo, *et al.*, High-performance photovoltaic perovskite layers fabricated through intramolecular exchange, *Science*, 2015, **348**(6240), 1234–1237.

3 D. Bi, W. Tress, M. I. Dar, P. Gao, J. Luo, C. Renevier, *et al.*, Efficient luminescent solar cells based on tailored mixed-cation perovskites, *Sci. Adv.*, 2016, **2**(1), e1501170.

4 M. Saliba, T. Matsui, J.-Y. Seo, K. Domanski, J.-P. Correa-Baena, M. K. Nazeeruddin, *et al.*, Cesium-containing triple cation perovskite solar cells: improved stability, reproducibility and high efficiency, *Energy Environ. Sci.*, 2016, **9**(6), 1989–1997.

5 J. P. Correa Baena, L. Steier, W. Tress, M. Saliba, S. Neutzner, T. Matsui, *et al.*, Highly efficient planar perovskite solar cells through band alignment engineering, *Energy Environ. Sci.*, 2015, **8**(10), 2928–2934.

6 J. Burschka, N. Pellet, S.-J. Moon, R. Humphry-Baker, P. Gao, M. K. Nazeeruddin, *et al.*, Sequential deposition as a route to high-performance perovskite-sensitized solar cells, *Nature*, 2013, **499**(7458), 316–319.

7 H. J. Snaith, A. Abate, J. M. Ball, G. E. Eperon, T. Leijtens, N. K. Noel, *et al.*, Anomalous hysteresis in perovskite solar cells, *J. Phys. Chem. Lett.*, 2014, **5**(9), 1511–1515.

8 E. L. Unger, E. T. Hoke, C. D. Bailie, W. H. Nguyen, A. R. Bowring, T. Heumuller, *et al.*, Hysteresis and transient behavior in current–voltage measurements of hybrid-perovskite absorber solar cells, *Energy Environ. Sci.*, 2014, **7**(11), 3690–3698.

9 G. Xing, B. Wu, S. Chen, J. Chua, N. Yantara, S. Mhaisalkar, *et al.*, Interfacial electron transfer barrier at compact TiO_2/$CH_3NH_3PbI_3$ heterojunction, *Small*, 2015, **11**(29), 3606–3613.

10 T. Leijtens, G. E. Eperon, S. Pathak, A. Abate, M. M. Lee and H. J. Snaith, Overcoming ultraviolet light instability of sensitized TiO_2 with meso-superstructured organometal tri-halide perovskite solar cells, *Nat. Commun.*, 2013, **4**, 2885.

11 S. Ito, S. Tanaka, K. Manabe and H. Nishino, Effects of surface blocking layer of Sb2S3 on nanocrystalline TiO_2 for $CH_3NH_3PbI_3$ perovskite solar cells, *J. Phys. Chem. C*, 2014, **118**(30), 16995–17000.

12 Z. Zhou, J. Xu, L. Xiao, J. Chen, T. Za, J. Yao, *et al.*, Efficient planar perovskite solar cells prepared *via* a low-pressure vapor-assisted solution process with fullerene/TiO_2 as an electron collection bilayer, *RSC Adv.*, 2016, **6**(82), 78585–78594.

13 K. Wojciechowski, S. D. Stranks, A. Abate, G. Sadoughi, A. Sadhanala, N. Kopidakis, *et al.*, Heterojunction modification for highly efficient organic–inorganic perovskite solar cells, *ACS Nano*, 2014, **8**(12), 12701–12709.

14 W. Ke, D. Zhao, C. R. Grice, A. J. Cimaroli, J. Ge, H. Tao, *et al.*, Efficient planar perovskite solar cells using room-temperature vacuum-processed C60 electron selective layers, *J. Mater. Chem. A*, 2015, **3**(35), 17971–17976.

15 C. Liu, K. Wang, P. Du, T. Meng, X. Yu, S. Z. D. Cheng, *et al.*, High Performance Planar Heterojunction Perovskite Solar Cells with Fullerene Derivatives as the Electron Transport Layer, *ACS Appl. Mater. Interfaces*, 2015, **7**(2), 1153–1159.

16 C. Tao, S. Neutzner, L. Colella, S. Marras, A. R. Srimath Kandada, M. Gandini, *et al.*, 17.6% stabilized efficiency in low-temperature processed planar perovskite solar cells, *Energy Environ. Sci.*, 2015, **8**(8), 2365–2370.

17 T. Cao, Z. Wang, Y. Xia, B. Song, Y. Zhou, N. Chen, *et al.*, Facilitating Electron Transportation in Perovskite Solar Cells *via* Water-Soluble Fullerenol Interlayers, *ACS Appl. Mater. Interfaces*, 2016, **8**(28), 18284–18291.

18 Y. Dong, W. Li, X. Zhang, Q. Xu, Q. Liu, C. Li, *et al.*, Highly Efficient Planar Perovskite Solar Cells *via* Interfacial Modification with Fullerene Derivatives, *Small*, 2016, **12**(8), 1098–1104.

19 Q. Xu, Z. Lu, L. Zhu, C. Kou, Y. Liu, C. Li, *et al.*, Elimination of the *J–V* hysteresis of planar perovskite solar cells by interfacial modification with a thermo-cleavable fullerene derivative, *J. Mater. Chem. A*, 2016, **4**(45), 17649–17654.

20 W. Qiu, J. P. Bastos, S. Dasgupta, T. Merckx, I. Cardinaletti, M. V. C. Jenart, et al., Highly efficient perovskite solar cells with crosslinked PCBM interlayers, J. Mater. Chem. A, 2017, 5(6), 2466–2472.

21 W. Zhou, J. Zhen, Q. Liu, Z. Fang, D. Li, P. Zhou, et al., Successive surface engineering of TiO$_2$ compact layers via dual modification of fullerene derivatives affording hysteresis-suppressed high-performance perovskite solar cells, J. Mater. Chem. A, 2017, 5(4), 1724–1733.

22 B. Li, Y. Chen, Z. Liang, D. Gao and W. Huang, Interfacial engineering by using self-assembled monolayer in mesoporous perovskite solar cell, RSC Adv., 2015, 5(114), 94290–94295.

23 W. Ke, D. Zhao, C. R. Grice, A. J. Cimaroli, G. Fang and Y. Yan, Efficient fully-vacuum-processed perovskite solar cells using copper phthalocyanine as hole selective layers, J. Mater. Chem. A, 2015, 3(47), 23888–23894.

24 K. Wojciechowski, T. Leijtens, S. Siprova, C. Schlueter, M. T. Hörantner, J. T.-W. Wang, et al., C60 as an Efficient n-Type Compact Layer in Perovskite Solar Cells, J. Phys. Chem. Lett., 2015, 6(12), 2399–2405.

25 D. Zhao, W. Ke, C. R. Grice, A. J. Cimaroli, X. Tan, M. Yang, et al., Annealing-free efficient vacuum-deposited planar perovskite solar cells with evaporated fullerenes as electron-selective layers, Nano Energy, 2016, 19, 88–97.

26 S. Chang, G. D. Han, J. G. Weis, H. Park, O. Hentz, Z. Zhao, et al., Transition Metal-Oxide Free Perovskite Solar Cells Enabled by a New Organic Charge Transport Layer, ACS Appl. Mater. Interfaces, 2016, 8(13), 8511–8519.

27 C.-Y. Chang, Y.-C. Chang, W.-K. Huang, W.-C. Liao, H. Wang, C. Yeh, et al., Achieving high efficiency and improved stability in large-area ITO-free perovskite solar cells with thiol-functionalized self-assembled monolayers, J. Mater. Chem. A, 2016, 4(20), 7903–7913.

28 H. Yoon, S. M. Kang, J.-K. Lee and M. Choi, Hysteresis-free low-temperature-processed planar perovskite solar cells with 19.1% efficiency, Energy Environ. Sci., 2016, 9(7), 2262–2266.

29 J. H. Kim, C.-C. Chueh, S. T. Williams and A. K. Y. Jen, Room-temperature, solution-processable organic electron extraction layer for high-performance planar heterojunction perovskite solar cells, Nanoscale, 2015, 7(41), 17343–17349.

30 S. Ryu, J. Seo, S. S. Shin, Y. C. Kim, N. J. Jeon, J. H. Noh, et al., Fabrication of metal-oxide-free CH$_3$NH$_3$PbI$_3$ perovskite solar cells processed at low temperature, J. Mater. Chem. A, 2015, 3(7), 3271–3275.

31 J. Ha, H. Kim, H. Lee, K.-G. Lim, T.-W. Lee and S. Yoo, Device architecture for efficient, low-hysteresis flexible perovskite solar cells: Replacing TiO$_2$ with C60 assisted by polyethylenimine ethoxylated interfacial layers, Sol. Energy Mater. Sol. Cells, 2017, 161, 338–346.

32 J. Xu, A. Buin, A. H. Ip, W. Li, O. Voznyy, R. Comin, et al., Perovskite–fullerene hybrid materials suppress hysteresis in planar diodes, Nat. Commun., 2015, 6, 7081.

33 C.-H. Chiang and C.-G. Wu, Bulk heterojunction perovskite–PCBM solar cells with high fill factor, Nat. Photonics, 2016, 10(3), 196–200.

34 S. Collavini, I. Kosta, S. F. Völker, G. Cabanero, H. J. Grande, R. Tena-Zaera, et al., Efficient Regular Perovskite Solar Cells Based on Pristine[70] Fullerene as Electron-Selective Contact, ChemSusChem, 2016, 9(11), 1263–1270.

35 J. Pascual, I. Kosta, T. Tuyen Ngo, A. Chuvilin, G. Cabanero, H. J. Grande, et al., Electron Transport Layer-Free Solar Cells Based on Perovskite-Fullerene Blend Films with Enhanced Performance and Stability, ChemSusChem, 2016, 9(18), 2679–2685.

36 L. Liu, A. Mei, T. Liu, P. Jiang, Y. Sheng, L. Zhang, et al., Fully Printable Mesoscopic Perovskite Solar Cells with Organic Silane Self-Assembled Monolayer, J. Am. Chem. Soc., 2015, 137(5), 1790–1793.

37 A. Abrusci, S. D. Stranks, P. Docampo, H.-L. Yip, A. K. Y. Jen and H. J. Snaith, High-Performance Perovskite-Polymer Hybrid Solar Cells via Electronic Coupling with Fullerene Monolayers, Nano Lett., 2013, 13(7), 3124–3128.

38 G. Yang, C. Wang, H. Lei, X. Zheng, P. Qin, L. Xiong, et al., Interface engineering in planar perovskite solar cells: energy level alignment, perovskite morphology control and high performance achievement, J. Mater. Chem. A, 2017, 5(4), 1658–1666.

39 P. Docampo, J. M. Ball, M. Darwich, G. E. Eperon and H. J. Snaith, Efficient organometal trihalide perovskite planar-heterojunction solar cells on flexible polymer substrates, Nat. Commun., 2013, 4, 2761.

40 J.-Y. Jeng, Y.-F. Chiang, M.-H. Lee, S.-R. Peng, T.-F. Guo, P. Chen, et al., CH$_3$NH$_3$PbI$_3$ Perovskite/Fullerene Planar-Heterojunction Hybrid Solar Cells, Adv. Mater., 2013, 25(27), 3727–3732.

41 O. Malinkiewicz, A. Yella, Y. H. Lee, G. M. Espallargas, M. Graetzel, M. K. Nazeeruddin, et al., Perovskite solar cells employing organic charge-transport layers, Nat. Photonics, 2013, 8(2), 128–132.

42 C.-H. Chiang, Z.-L. Tseng and C.-G. Wu, Planar heterojunction perovskite/PC71BM solar cells with enhanced open-circuit voltage via a (2/1)-step spin-coating process, J. Mater. Chem. A, 2014, 2(38), 15897–15903.

43 Q. Lin, A. Armin, R. C. R. Nagiri, P. L. Burn and P. Meredith, Electro-optics of perovskite solar cells, Nat. Photonics, 2014, 9(2), 106–112.

44 J. Seo, S. Park, Y. Chan Kim, N. J. Jeon, J. H. Noh, S. C. Yoon, et al., Benefits of very thin PCBM and LiF layers for solution-processed p–i–n perovskite solar cells, Energy Environ. Sci., 2014, 7(8), 2642.

45 S. Sun, T. Salim, N. Mathews, M. Duchamp, C. Boothroyd, G. Xing, et al., The origin of high efficiency in low-temperature solution-processable bilayer organometal halide hybrid solar cells, Energy Environ. Sci., 2014, 7(1), 399–407.

46 Q. Wang, Y. Shao, Q. Dong, Z. Xiao, Y. Yuan and J. Huang, Large fill-factor bilayer iodine perovskite solar cells fabricated by a low-temperature solution-process, Energy Environ. Sci., 2014, 7(7), 2359–2365.

47 J. You, Z. Hong, Y. Yang, Q. Chen, M. Cai, T.-B. Song, *et al.*, Low-Temperature Solution-Processed Perovskite Solar Cells with High Efficiency and Flexibility, *ACS Nano*, 2014, **8**(2), 1674–1680.

48 H. Azimi, T. Ameri, H. Zhang, Y. Hou, C. O. R. Quiroz, J. Min, *et al.*, A Universal Interface Layer Based on an Amine-Functionalized Fullerene Derivative with Dual Functionality for Efficient Solution Processed Organic and Perovskite Solar Cells, *Adv. Energy Mater.*, 2015, **5**(8), 1401692.

49 J. H. Heo, H. J. Han, D. Kim, T. K. Ahn and S. H. Im, Hysteresis-less inverted $CH_3NH_3PbI_3$ planar perovskite hybrid solar cells with 18.1% power conversion efficiency, *Energy Environ. Sci.*, 2015, **8**(5), 1602–1608.

50 P.-W. Liang, C.-C. Chueh, S. T. Williams and A. K. Y. Jen, Roles of Fullerene-Based Interlayers in Enhancing the Performance of Organometal Perovskite Thin-Film Solar Cells, *Adv. Energy Mater.*, 2015, **5**(10), 1402321.

51 Y. Bai, Q. Dong, Y. Shao, Y. Deng, Q. Wang, L. Shen, *et al.*, Enhancing stability and efficiency of perovskite solar cells with crosslinkable silane-functionalized and doped fullerene, *Nat. Commun.*, 2016, **7**, 12806.

52 Y. Shao, Z. Xiao, C. Bi, Y. Yuan and J. Huang, Origin and elimination of photocurrent hysteresis by fullerene passivation in $CH_3NH_3PbI_3$ planar heterojunction solar cells, *Nat. Commun.*, 2014, **5**, 5784.

53 Y. Xing, C. Sun, H. L. Yip, G. C. Bazan, F. Huang and Y. Cao, New fullerene design enables efficient passivation of surface traps in high performance p–i–n heterojunction perovskite solar cells, *Nano Energy*, 2016, **26**, 7–15.

54 J. G. Matisons, Silanes and Siloxanes as Coupling Agents to Glass: A Perspective, in *Silicone Surface Science*, ed. J. M. Owen and R. P. Dvornic, Springer, Dordrecht, Netherlands, 2012, pp. 281–298.

55 B. Arkles, J. R. Steinmetz, J. Zazyczny and P. Mehta, Factors contributing to the stability of alkoxysilanes in aqueous solution, *J. Adhes. Sci. Technol.*, 1992, **6**(1), 193–206.

56 A. Bianco, F. Gasparrini, M. Maggini, D. Misiti, A. Polese, M. Prato, *et al.*, Molecular Recognition by a Silica-Bound Fullerene Derivative, *J. Am. Chem. Soc.*, 1997, **119**(32), 7550–7554.

57 A. Baptiste, A. Gibaud, J. F. Bardeau, K. Wen, R. Maoz, J. Sagiv, *et al.*, X-ray, Micro-Raman, and Infrared Spectroscopy Structural Characterization of Self-Assembled Multilayer Silane Films with Variable Numbers of Stacked Layers, *Langmuir*, 2002, **18**(10), 3916–3922.

58 P. Innocenzi, P. Falcaro, S. Schergna, M. Maggini, E. Menna, H. Amenitsch, *et al.*, One-pot self-assembly of mesostructured silica films and membranes functionalised with fullerene derivatives, *J. Mater. Chem.*, 2004, **14**(12), 1838–1842.

59 K. Wojciechowski, I. Ramirez, T. Gorisse, O. Dautel, R. Dasari, N. Sakai, *et al.*, Cross-Linkable Fullerene Derivatives for Solution-Processed n–i–p Perovskite Solar Cells, *ACS Energy Lett.*, 2016, **1**(4), 648–653.

60 N. J. Jeon, J. H. Noh, Y. C. Kim, W. S. Yang, S. Ryu and S. I. Seok, Solvent engineering for high-performance inorganic–organic hybrid perovskite solar cells, *Nat. Mater.*, 2014, **13**(9), 897–903.

61 M. Xiao, F. Huang, W. Huang, Y. Dkhissi, Y. Zhu, J. Etheridge, *et al.*, A Fast Deposition-Crystallization Procedure for Highly Efficient Lead Iodide Perovskite Thin-Film Solar Cells, *Angew. Chem., Int. Ed.*, 2014, **53**(37), 9898–9903.

62 H. J. Snaith, How should you measure your excitonic solar cells?, *Energy Environ. Sci.*, 2012, **5**(4), 6513.

63 M. J. Frisch, G. W. Trucks, H. B. Schlegel, G. E. Scuseria, M. A. Robb, J. R. Cheeseman, *et al.*, *Gaussian 09*, Gaussian, Inc., Wallingford, CT, USA, 2009.

64 D. Nečas and P. Klapetek, Gwyddion: an open-source software for SPM data analysis, *Open Phys.*, 2012, **10**(1).

65 W. Nie, H. Tsai, R. Asadpour, J.-C. Blancon, A. J. Neukirch, G. Gupta, *et al.*, High-efficiency solution-processed perovskite solar cells with millimeter-scale grains, *Science*, 2015, **347**(6221), 522–525.

66 H. Tsai, W. Nie, J.-C. Blancon, C. C. Stoumpos, R. Asadpour, B. Harutyunyan, *et al.*, High-efficiency two-dimensional Ruddlesden–Popper perovskite solar cells, *Nature*, 2016, **536**(7616), 312–316.

67 Z. Xiao, C. Bi, Y. Shao, Q. Dong, Q. Wang, Y. Yuan, *et al.*, Efficient, high yield perovskite photovoltaic devices grown by interdiffusion of solution-processed precursor stacking layers, *Energy Environ. Sci.*, 2014, **7**(8), 2619–2623.

68 F. Lamberti, L. Brigo, M. Favaro, C. Luni, A. Zoso, M. Cattelan, *et al.*, Optoelectrochemical Biorecognition by Optically Transparent Highly Conductive Graphene-Modified Fluorine–Doped Tin Oxide Substrates, *ACS Appl. Mater. Interfaces*, 2014, **6**(24), 22769–22777.

69 B. Roose, J.-P. C. Baena, K. C. Gödel, M. Graetzel, A. Hagfeldt, U. Steiner, *et al.*, Mesoporous SnO_2 electron selective contact enables UV-stable perovskite solar cells, *Nano Energy*, 2016, **30**, 517–522.

70 R. Zhang, L. Wang and W. Shi, Variable corrosion behavior of a thick amorphous carbon coating in NaCl solution, *RSC Adv.*, 2015, **5**(116), 95750–95763.

71 S. A. McCluney, S. N. Popova, B. N. Popov, R. E. White and R. B. Griffin, Comparing Electrochemical Impedance Spectroscopy Methods for Estimating the Degree of Delamination of Organic Coatings on Steel, *J. Electrochem. Soc.*, 1992, **139**(6), 1556–1560.

72 M. E. Orazem and B. Tribollet, *Electrochemical Impedance Spectroscopy*, John Wiley & Sons, 2011.

73 G. Sánchez-Pomales, L. Santiago-Rodríguez, N. E. Rivera-Vélez and C. R. Cabrera, Control of DNA self-assembled monolayers surface coverage by electrochemical desorption, *J. Electroanal. Chem.*, 2007, **611**(1–2), 80–86.

74 F. Jahani, S. Torabi, R. C. Chiechi, L. J. A. Koster and J. C. Hummelen, Fullerene derivatives with increased dielectric constants, *Chem. Commun.*, 2014, **50**(73), 10645–10647.

75 J. F. Rubinson and Y. P. Kayinamura, Charge transport in conducting polymers: insights from impedance spectroscopy, *Chem. Soc. Rev.*, 2009, **38**(12), 3339–3347.

11892 | *J. Mater. Chem. A*, 2017, **5**, 11882–11893

This journal is © The Royal Society of Chemistry 2017

76 Z. Li, M. Yang, J.-S. Park, S.-H. Wei, J. J. Berry and K. Zhu, Stabilizing Perovskite Structures by Tuning Tolerance Factor: Formation of Formamidinium and Cesium Lead Iodide Solid-State Alloys, *Chem. Mater.*, 2016, **28**(1), 284–292.

77 Z. Xiao, Q. Dong, C. Bi, Y. Shao, Y. Yuan and J. Huang, Solvent Annealing of Perovskite-Induced Crystal Growth for Photovoltaic-Device Efficiency Enhancement, *Adv. Mater.*, 2014, **26**(37), 6503–6509.

78 H. D. Kim, H. Ohkita, H. Benten and S. Ito, Photovoltaic Performance of Perovskite Solar Cells with Different Grain Sizes, *Adv. Mater.*, 2016, **28**(5), 917–922.

79 C. Bi, Q. Wang, Y. Shao, Y. Yuan, Z. Xiao and J. Huang, Non-wetting surface-driven high-aspect-ratio crystalline grain growth for efficient hybrid perovskite solar cells, *Nat. Commun.*, 2015, **6**, 7747.

80 E. H. Anaraki, A. Kermanpur, L. Steier, K. Domanski, T. Matsui, W. Tress, *et al.*, Highly efficient and stable planar perovskite solar cells by solution-processed tin oxide, *Energy Environ. Sci.*, 2016, **9**(10), 3128–3134.

81 S. van Reenen, M. Kemerink and H. J. Snaith, Modeling Anomalous Hysteresis in Perovskite Solar Cells, *J. Phys. Chem. Lett.*, 2015, **6**(19), 3808–3814.

82 A. Guerrero, B. Dörling, T. Ripolles-Sanchis, M. Aghamohammadi, E. Barrena, M. Campoy-Quiles, *et al.*, Interplay between Fullerene Surface Coverage and Contact Selectivity of Cathode Interfaces in Organic Solar Cells, *ACS Nano*, 2013, **7**(5), 4637–4646.

83 Uv test for photovoltaic (PC) modules, TC 82-Solar photovoltaic energy systems, 1998.